Elastic propagation of fast electron vortices through crystals

Stefan Löffler[a]* and Peter Schattschneider[a,b]

[a]Institute of Solid State Physics, Vienna University of Technology, Wiedner Hauptstrasse 8-10, 1040 Vienna, Austria, and [b]University Service Center for Transmission Electron Microscopy, Vienna University of Technology, Wiedner Hauptstrasse 8-10, 1040 Vienna, Austria. Correspondence e-mail: stefan.loeffler@tuwien.ac.at

The propagation of electron beams carrying angular momentum in crystals is studied using a multislice approach for the model system Fe. It is found that the vortex beam is distorted strongly due to elastic scattering. Consequently, the expectation value of the angular momentum as well as the local vortex components change with the initial position of the vortex and the propagation depth, making numerical simulations indispensable when analysing experiments.

1. Introduction

Recently, electron beams carrying topological charge have been created successfully in the transmission electron microscope (Verbeeck *et al.*, 2010; Uchida & Tonomura, 2010). The potential applications of these vortex beams (as they were called) seem endless – the speculation is that they will become as versatile a tool as vortices in optics (Molina-Terriza *et al.*, 2007). In particular, the proposed applications range from a strongly enhanced energy-loss magnetic chiral dichroism (EMCD) (Schattschneider *et al.*, 2006) signal over the probing of chiral structures to the manipulation of nanoparticles (Xin & Muller, 2010).

One essential aspect of electron beams has been overlooked so far, though, which is of paramount importance to real experiments. It is well known that, owing to the strong and long-ranged Coulomb interaction, the probe electrons in a sample undergo strong elastic scattering which depends heavily on aspects such as beam orientation or sample thickness (Williams & Carter, 1996; Löffler, 2011). This can be exploited as in high-resolution transmission electron microscopy (HRTEM) (Williams & Carter, 1996), atom location by channelling-enhanced microanalysis (ALCHEMI) (Spence & Taftø, 1983; Morimura & Hasaka, 2006), or energy-loss by channelled electrons (ELCE) (Krivanek *et al.*, 1982; Taftø & Spence, 1982). Recently, the new real-space scanning transmission electron microscopy (RSTEM) technique was used to map the effect of elastic scattering on a focused electron beam with sub-ångstrom precision (Etheridge *et al.*, 2011).

In other cases, such as EMCD, it is usually detrimental to the signal strength (Rusz *et al.*, 2007; Löffler *et al.*, 2011). In all cases, however, it plays an important role, and the same is to be expected for electron vortex beams (Löffler, 2011).

2. Simulations

In this work, we concentrate on the propagation of electron vortices that have been focused on the specimen, *i.e.* vortices produced as a convergent beam hitting the specimen. This corresponds to the situation of a holographic or phase plate in the condenser system of a transmission electron microscope (Schattschneider & Verbeeck, 2011; Schattschneider *et al.*, 2011; Verbeeck *et al.*, 2011, 2012). It must be emphasized, however, that the same results also apply to vortex beams that emanate from some point within the sample, *e.g.* after a chiral excitation as in EMCD.

In the case of a vortex produced by a condenser aperture, we can model the wave in the condenser plane as (Schattschneider & Verbeeck, 2011)

$$\tilde{\psi}(q, \varphi) = \exp(im\varphi)\Theta(q_{max} - q), \tag{1}$$

where $m = 1$ is the topological charge, φ is the polar angle in the condenser plane, q is the radial vector in the condenser plane, q_{max} is the radius of the aperture (which defines the maximum convergence angle), and $\Theta(x)$ is the Heaviside function. In the focused case (ignoring aberrations), the wavefunction ψ hitting the sample is given by the Fourier transformation of $\tilde{\psi}$, which corresponds to the Hankel transformation in polar coordinates (Schattschneider *et al.*, 2011):

$$\psi(r, \varphi) = \frac{i \exp(i\varphi)}{2\pi} \int_{0}^{q_{max}} J_1(qr)q \, dq$$
$$= \frac{iq_{max} \exp(i\varphi)}{4r} [J_1(q_{max}r)H_0(q_{max}r) - J_0(q_{max}r)H_1(q_{max}r)]. \tag{2}$$

Here, we use the Bessel functions of the first kind (J_m) and the Struve functions (H_m).

As a model system, we have chosen Fe. On the one hand, it has a simple crystal structure (body-centred cubic), on the other hand it is an easily accessible sample material and of general interest as a ferromagnetic model system.[1] In particular, we investigated the [001] zone axis which is a high-symmetry zone axis as can be seen from Fig. 1.

For the simulations, the focused vortex beam was positioned on four different positions on the crystal (see Fig. 1): on an atomic column (A), between the two closest atomic columns (B), as far away from atomic columns as possible (C), and in another, non-symmetric place (D). In all cases, a thickness of 200 Å and a spherical aberration coefficient $C_S = 0$ were assumed. Furthermore, an energy of 200 keV, an angular momentum of $\hbar$ and a convergence semi-angle of 9 mrad (corresponding to a waist radius of $\simeq 1.08$ Å) were used for the incident electron beam.

This electron beam was subsequently propagated through the crystal using the multislice approach[2] (Kirkland, 1998; Zauner, 2010; Dwyer & Etheridge, 2003) as is shown in Fig. 2. Fig. 3 shows the propagated wavefunctions at the exit plane. From them, it is obvious that (a) the wavefunctions generally no longer show the typical vortex phase and amplitude structure (Schattschneider & Verbeeck, 2011), (b) the structure – and in particular the phase distribution – depends critically on the initial position of the focused vortex with respect to the crystal, and (c) we generally see curved structures as one would expect for vortices, but which are absent in normal scanning transmission electron microscopy (STEM) (Dwyer & Etheridge, 2003).

In addition to the curved features between the atomic columns, the simulations shown in Fig. 3 also reproduce the channelling and dechannelling effects usually seen with focused electron beams (Dwyer & Etheridge, 2003). As a consequence, one sees significant intensity not only close to the initially illuminated atomic column, but also on the nearest and next-nearest neighbouring columns. Moreover, the central vortex phase structure is relatively well preserved in-between the atomic columns, even after a 200 Å-thick sample. In close proximity of the atomic columns, it is heavily distorted, however, which also leads to very different local phases at and around neighbouring atoms.

It must be noted here that all the images in Fig. 3 display the wavefunctions directly at the exit plane of the sample. If one wants to observe such patterns experimentally in a microscope, one has to use some post-specimen lens system to transfer those wavefunctions to the camera. These lens systems are usually not ideal and hence can introduce artifacts or obscure some details. Since the important object for all
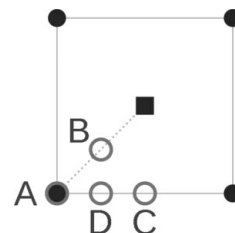

Figure 1
Projection of an Fe crystal in the [001] direction. Atoms in one layer are shown as discs and atoms in the other layer are shown as squares. The positions mentioned in the text are marked by capital letters. The edge length of the square is the lattice constant of Fe, namely 2.859 Å.

interactions in the sample is the wavefunction, however, it is more appropriate to show this directly, rather than the image one would get on a camera.

Recently, the feasibility of recording images similar to those shown in Fig. 3 was also demonstrated experimentally using the new RSTEM technique (Etheridge *et al.*, 2011). In combination with a next-generation, double-corrected transmission electron microscope, this technique can be used to investigate the real-space image of a focused electron beam with sub-ångstrom resolution after it has traversed the crystal.

3. Angular momentum

One of the most important characteristics of a vortex beam is its angular momentum. As helical wavefunctions are eigenstates of the $\hat{L}_z$ operator (Schattschneider & Verbeeck, 2011), they have a well defined, integer angular momentum quantum number m which is a constant of motion in free space. In fact, it is precisely this quantum number that defines the 'vorticity' of the beam. But how does it behave inside the sample?

Fig. 4 shows the evolution of the expectation value $\langle \hat{L}_z \rangle$ of the angular momentum as a function of depth z in the crystal. It is clearly obvious that (a) it changes significantly as the probe propagates through the crystal, (b) it is generally not an integer and can even surpass the initial value of $\hbar$, and (c) it is position dependent.

All of this can be explained by looking at the properties of $\hat{L}_z$. While this operator commutes with spherical operators such as the free-space Hamiltonian, it does not generally commute with the crystal Hamiltonian in which the spherical symmetry is broken by the crystal potential. Thus, $\langle \hat{L}_z \rangle$ is constant in free space, but can and will change inside a crystal. This also implies that the probe inside the crystal will evolve into a (coherent) superposition of different eigenstates of $\hat{L}_z$ over time, accounting for the non-integer expectation values.

Physically, this can be understood as an exchange of angular momentum between the probe beam and the crystal. Because of the very different masses of probe electron and sample as well as the oscillatory nature[3] of $\langle \hat{L}_z \rangle$ in Fig. 4, the change of the angular momentum of the sample usually is not measur-

---

[1] The effect of the internal magnetic field on the probe was ignored in this work, however, as is common procedure in elastic calculations.
[2] The simulation area was 512×512 pixels^2 or 45.744×45.744 Å^2, corresponding to 16×16 unit cells. The slice thickness was 1.4295 Å, corresponding to half a unit-cell height. For the sake of simplicity and calculation speed, quasi-elastic scattering (*i.e.* interaction with phonons) and inelastic scattering were neglected.

[3] Interestingly, the period length of $\simeq 8$ nm of the $\langle \hat{L}_z \rangle$ oscillations is of the same order of magnitude as the $\simeq 10$ nm period length of the *Pendellösung*.
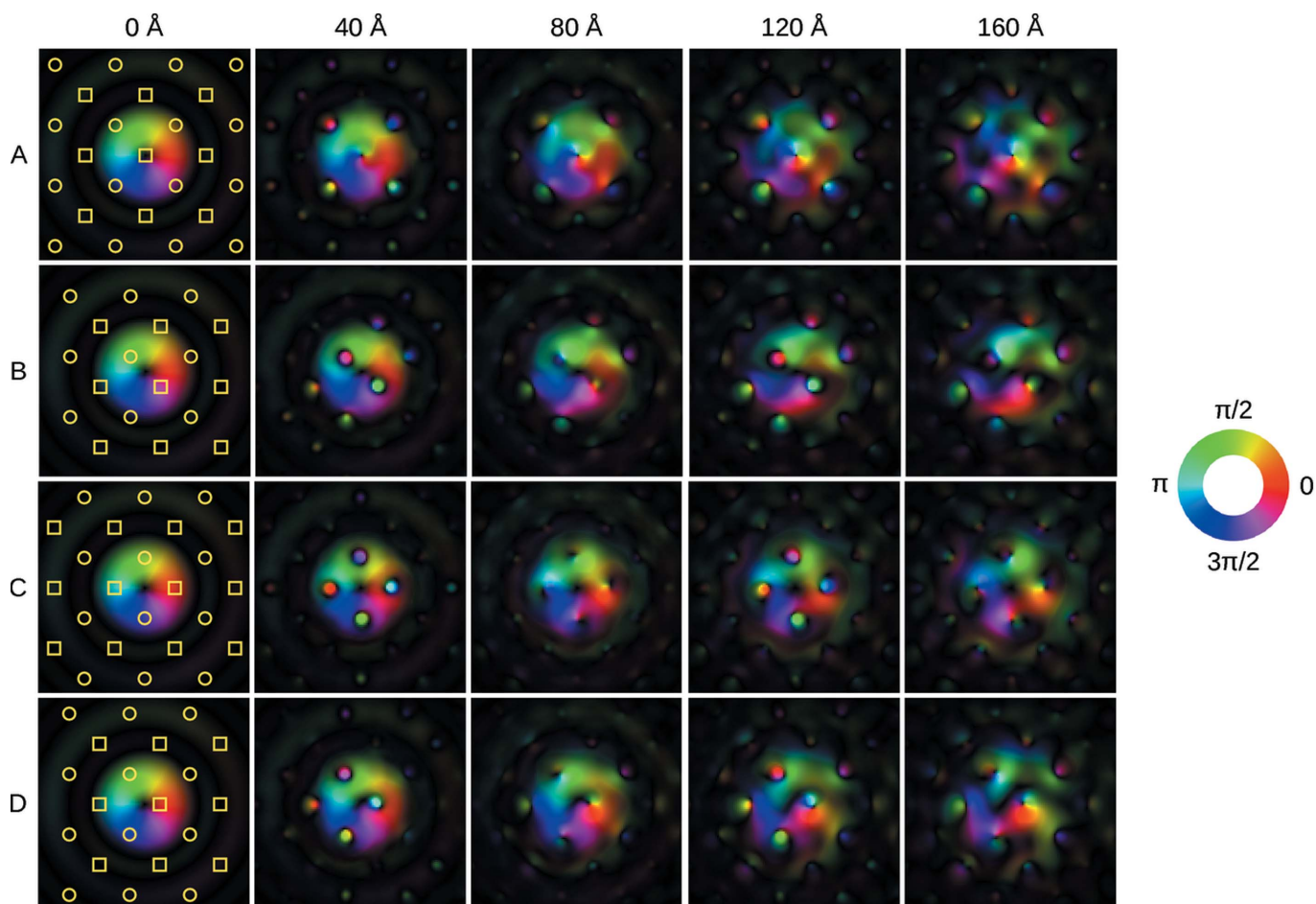
Figure 2
Wavefunctions at different depths z (as noted above the columns; the wave at the exit surface at $z = 200$ Å is given in Fig. 3) in the Fe crystal for the positions A, B, C and D as defined in the text and in Fig. 1. For $z = 0$ Å, the atom positions are superimposed on the incident wave. The two different symbols mark the positions of Fe atoms in the two different layers of the unit cell. All images show the real-space amplitudes (brightness) and phases (hue, as specified in the colour wheel on the right) for a $(10$ Å$)^2$ subset of the simulated data.

able. For nanoparticles of suitable sizes, however, this could produce appreciable angular velocities.

From this physical interpretation, the position dependence is understandable as well. If the (ångstrom-sized) probe is positioned directly on an atom column, it usually channels down along that column, whereas a similar probe positioned between columns will first spread until it hits several columns at once and will subsequently channel down primarily along those (Dwyer & Etheridge, 2003). Therefore, the amount the focused probe beam interacts with the sample obviously depends on its position, as is readily visible in Fig. 4.

4. Vortex decomposition

In the previous section, we have seen that inside the sample, a pure vortex state evolves into a coherent superposition of such states. In fact, the occurrence of different vortex components is not an effect unique to a crystal – even in free space, a vortex wave can be described by a single $\exp(im\varphi)$ function (with polar angle φ) only in a single cylindrical coordinate system, namely the one for which the z axis coincides with the

propagation axis of the phase singularity in the centre of the vortex. If the vortex is displaced relative to the origin of the coordinate system, again several components come into play, as can readily be seen from Fig. 5. Only if we describe the $m = 1$ vortex centred on position A around that very position do we retrieve exclusively an $m = 1$ component. In all other cases, additional components are mixed in, including $m = 0$ Airy-like components and even opposite $m = -1$ components.

In free space, all these components add up to a single (displaced) vortex wave which has a well defined and, most importantly, constant angular momentum.[4] In a crystal, however, this is no longer the case, and consequently the relative weights of the different components change with the penetration depth in the crystal, just as $\langle \hat{L}_z \rangle$ changes.

Fig. 6 shows how the most important local amplitude components around the atom at position A change with depth, dependent on the vortex position. For this, the vortex was

---

[4] It can readily be seen that, similar to the parallel axis theorem in classical mechanics, $\langle \hat{L}_z \rangle = m\hbar + i\hbar \mathbf{r}_0 \times \langle \hat{\mathbf{p}} \rangle$ under a displacement $\mathbf{r}_0$.
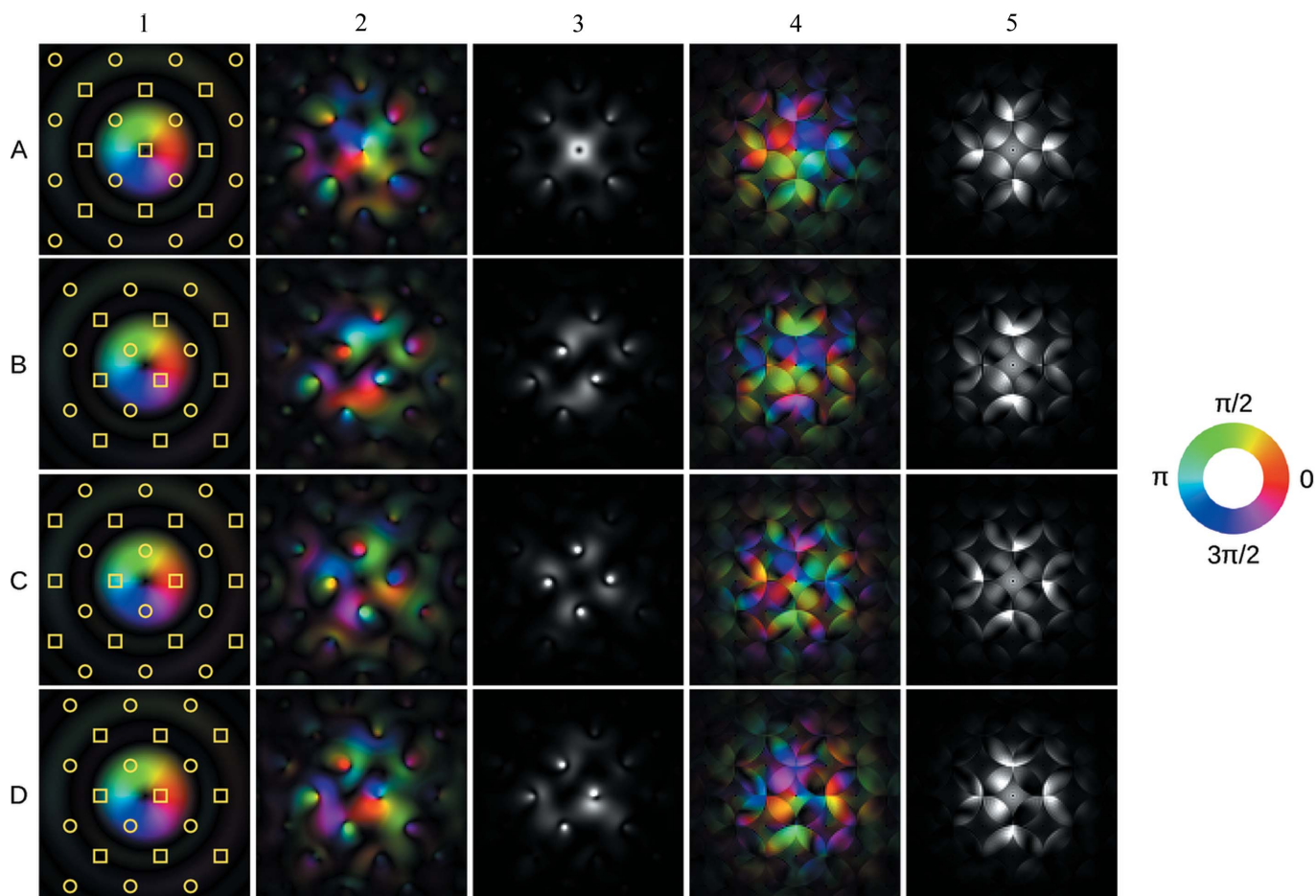
Figure 3
Wavefunctions at the entrance plane (column 1) and the exit plane (columns 2–5) of the 20 nm-thick Fe sample for the positions A, B, C and D as defined in the text and in Fig. 1. Column 1 shows the atom positions superimposed on the incident wave. The two different symbols mark the positions of Fe atoms in the two different layers of the unit cell. Column 2 shows the real-space amplitudes (brightness) and phases (hue, as specified in the colour wheel on the right), column 3 shows the corresponding intensities, column 4 shows the reciprocal-space amplitudes and phases, and column 5 shows the diffraction intensities. Columns 1–3 show a $(10 \text{ Å})^2$ subset of the simulated data, while columns 4–5 show a $(2.45 \text{ Å}^{-1})^2$ subset.
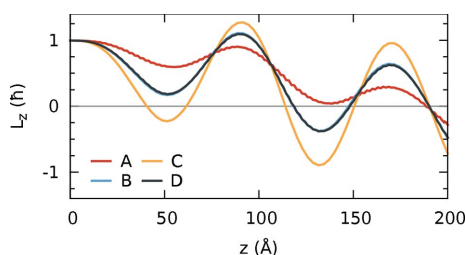

Figure 4
Expectation value $\langle \hat{L}_z \rangle$ in Fe [001] for the four positions given in the text and in Fig. 1 as a function of penetration depth z. The curves for positions B and D overlap.

propagated with an initial position A–D. At each depth, the wavefunction was decomposed in vortex components around the atom A, and the amplitude at the radius $r = 1.08$ Å (which corresponds to the nominal beam waist radius) was extracted. As such, $z = 0$ in Fig. 6 corresponds to $r = 1.08$ Å in Fig. 5.

It is readily visible from Fig. 6 that the local vortex amplitudes change with thickness, but the precise behaviour

depends crucially on the initial vortex position and the vortex order of interest. The oscillatory behaviour seen best in the curves for A/$m = 1$, D/$m = 1$ and D/$m = 2$ is reminiscent of the *Pendellösung* of conventional Bloch waves, although an analytical equation for its description is unfeasible because each vortex contains infinitely many Bloch-wave components.

5. Conclusion

The calculations shown in the previous sections show that one has to be careful when predicting or interpreting the effects of vortices if they pass through matter. In particular, statements one usually takes for granted when dealing with vortices – such as the conservation of topological charge or equivalently angular momentum – are only valid in free space. Inside a sample, electron vortex beams can be heavily distorted, which will change the components present in a local environment around the atom. As a consequence, one can have $m = 0$ and $m = 2$ beams in the vicinity of a scattering atom, even if the original vortex had $m = 1$.
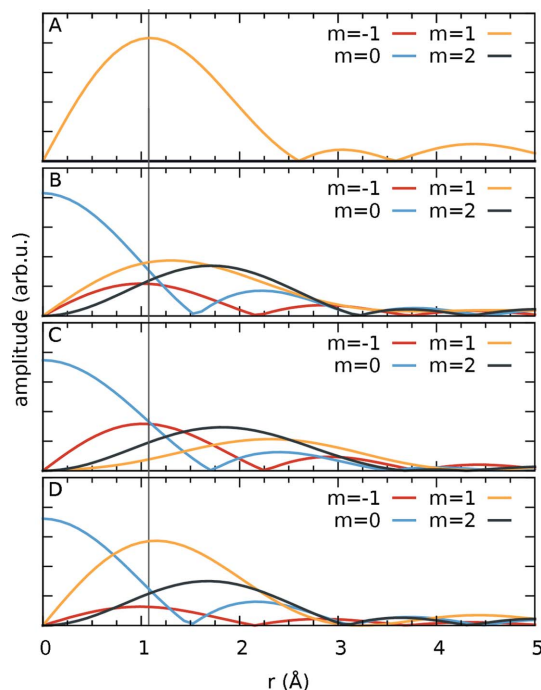
Figure 5
Expansion of an $m = 1$ vortex incident on position A for the positions A–D given in the text. Only the most important components $m = -1, 0, 1, 2$ are plotted. The scale is the same in all subfigures. The vertical line marks the nominal beam waist radius that was used to calculate the depth plots in Fig. 6.

Figure 6
Dependence of the local amplitudes of the most important vortex components $m = -1, 0, 1, 2$ for vortices positioned at the positions A–D given in the text on the depth z in the crystal. The local amplitudes were calculated at a radius of $r = 1.08$ Å (which corresponds to the nominal beam waist radius) around the atom at position A. The scale in all subfigures is the same as in Fig. 5.

This creates new challenges for the use of vortices in, *e.g.*, EMCD, but at the same time provides new, exciting possibilities. These range from the conversion of vortex beams from one topological charge to another, to the transfer of angular momentum to nanoparticles.

References

Dwyer, C. & Etheridge, J. (2003). *Ultramicroscopy*, **96**, 343–360.
Etheridge, J., Lazar, S., Dwyer, C. & Botton, G. A. (2011). *Phys. Rev. Lett.* **106**, 160802.
Kirkland, E. J. (1998). *Advanced Computing in Electron Microscopy*. New York: Plenum Press.
Krivanek, O. L., Disko, M. M., Taftø, J. & Spence, J. C. H. (1982). *Ultramicroscopy*, **9**, 249–254.
Löffler, S. (2011). In *Proceedings of the Microscopy Conference 2011, Kiel, Germany*, Vol. 1. Düsseldorf: Deutsche Gesellschaft für Elektronenmikroskopie e.V.
Löffler, S., Ennen, I., Tian, F., Schattschneider, P. & Jaouen, N. (2011). *Ultramicroscopy*, **111**, 1163–1167.
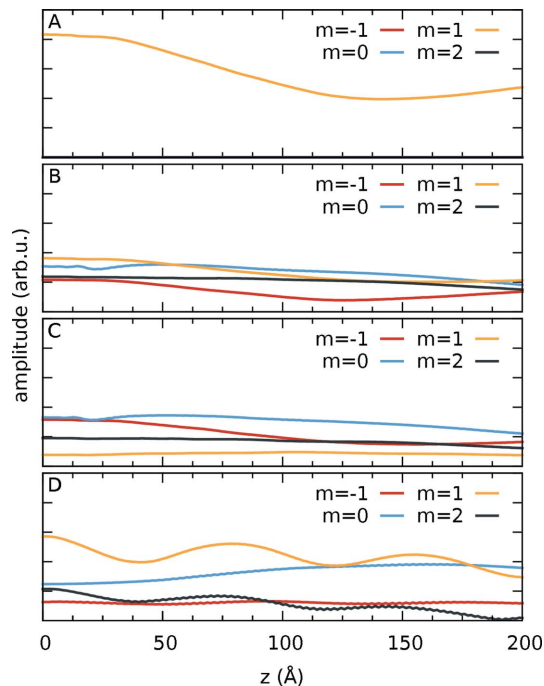
Molina-Terriza, G., Torres, J. P. & Torner, L. (2007). *Nat. Phys.* **3**, 305–310.
Morimura, T. & Hasaka, M. (2006). *Ultramicroscopy*, **106**, 553–560.
Rusz, J., Rubino, S. & Schattschneider, P. (2007). *Phys. Rev. B*, **75**, 214425.
Schattschneider, P., Rubino, S., Hebert, C., Rusz, J., Kunes, J., Novák, P., Carlino, E., Fabrizioli, M., Panaccione, G. & Rossi, G. (2006). *Nature (London)*, **441**, 486–488.
Schattschneider, P., Stöger-Pollach, M., Löffler, S., Steiger-Thirsfeld, A., Hell, J. & Verbeeck, J. (2011). *Ultramicroscopy*, **115**, 21–25.
Schattschneider, P. & Verbeeck, J. (2011). *Ultramicroscopy*, **111**, 1461–1468.
Spence, J. C. H. & Taftø, J. (1983). *J. Microsc.* **130**, 147–154.
Taftø, J. & Spence, J. C. (1982). *Science*, **218**, 49–51.
Uchida, M. & Tonomura, A. (2010). *Nature (London)*, **464**, 737–739.
Verbeeck, J., Schattschneider, P., Lazar, S., Stöger-Pollach, M., Löffler, S., Steiger-Thirsfeld, A. & Van Tendeloo, G. (2011). *Appl. Phys. Lett.* **99**, 203109.
Verbeeck, J., Tian, H. & Béché, A. (2012). *Ultramicroscopy*, **113**, 83–87.
Verbeeck, J., Tian, H. & Schattschneider, P. (2010). *Nature (London)*, **467**, 301–304.
Williams, D. B. & Carter, C. B. (1996). *Transmission Electron Microscopy*. New York: Plenum Press.
Xin, H. L. & Muller, D. A. (2010). *Nat. Nanotechnol.* **5**, 764–765.
Zauner, M. (2010). MSc thesis, Vienna University of Technology, Austria.